California State University, Monterey Bay

Digital Commons @ CSUMB

Summer 2019

Contributions of Wind- and Wave-Induced Transport to Nearshore Phytoplankton Variability in Northern California

Patrick C. Daniel
California State University, Monterey Bay

Follow this and additional works at: https://digitalcommons.csumb.edu/caps_thes_all

CONTRIBUTIONS OF WIND- AND WAVE-INDUCED TRANSPORT TO

NEARSHORE PHYTOPLANKTON VARIABILITY IN NORTHERN CALIFORNIA

_____

A Thesis

Presented to the

Faculty of

Moss Landing Marine Laboratories

California State University Monterey Bay

_____

In Partial Fulfillment

of the Requirements for the Degree

Master of Science

in

Marine Science

_____

by

Patrick C. Daniel

Summer 2019

CALIFORNIA STATE UNIVERSITY MONTEREY BAY

The Undersigned Faculty Committee Approves the

Thesis of Patrick C. Daniel:

CONTRIBUTIONS OF WIND- AND WAVE-INDUCED TRANSPORT TO

NEARSHORE PHYTOPLANKTON VARIABILITY IN NORTHERN

CALIFORNIA

_____
Thomas Connolly, Chair
Moss Landing Marine Laboratories

_____
Colleen Durkin
Moss Landing Marine Laboratories

_____
Nicholas Welschmeyer
Moss Landing Marine Laboratories

Approved by the Dean of Graduate Studies
_____
Kris Roney, Dean
Associate VP for Academic Programs and Dean of Undergraduate and Graduate Studies

_____
08/12/2019
Approval Date

For Kate, Chris, Josh, and George.

Is there anyone who can watch without fascination the struggle for supremacy between sea and land?

- Willard Bascom, *Waves and Beaches 2nd Edition,* 1980

ABSTRACT

Contribitions of Wind- and Wave-Induced Transport to Nearshore
Phytoplankton Variability in Northern California
by
Patrick C. Daniel
Master of Science in Marine Science
California State University Monterey Bay, 2019

Phytoplankton form the base of the marine food web and provide important subsidies to the nearshore and intertidal communities. In the California Current Ecosystem (CCE), high phytoplankton abundance is largely attributed to seasonal equatorward alongshore winds which drive coastal upwelling. At shorter temporal and spatial scales, nearshore phytoplankton abundance is highly variable and sensitive to local oceanographic conditions and the influence of wave-induced interactions. Between 2008 to 2012, periods of rapid onset high phytoplankton abundance (n=41) were identified during the upwelling season (March to October) in the intertidal environment of Bodega Head, in Northern California. The rapid accumulation of phytoplankton occurred at short latencies (~20 hours) and was correlated with increases in offshore alongshore wind stress and significant wave height. Wave-induced transport, known as Stokes drift, was calculated from a nearshore wave model, providing a physical mechanism to advect and trap phytoplankton in the nearshore. A surface particle tracking model forced by High-Frequency Radar-derived surface currents revealed that the majority of water masses during the high phytoplankton events originated from offshore to the north, suggesting that waters originated from the Point Arena upwelling center. Stokes drift, which is reinforced by alongshore winds, provides a transport mechanism for linking large scale offshore processes with the nearshore environment. This study underscores the importance of considering Stokes drift when examining biophysical interactions in the nearshore environment.

TABLE OF CONTENTS

LIST OF TABLES

PAGE

LIST OF FIGURES

PAGE

ACKNOWLEDGEMENTS

The first and largest acknowledgement for this work must be to my advisor Prof. Tom Connolly. His enthusiasm and support for my growth as an oceanographer and as a person has been invaluable. He has shown nearly endless patience as I grappled with processes in the physical oceanography and let my curiosities lead me a stray from completing my thesis. I am constantly inspired with Tom's wide berth of his academic interests, his ability to elucidate complex topics, and his dedication to his students. The rest of my committee, Dr. Colleen Durkin and Prof. Nick Welschmeyer provided meaningful insight into biological processes and invaluable advice on the structure of this thesis. They both also provided validation and encouragement in times of need. This work would not have been possible without the Central and Northern California Ocean Observing System (CeNCOOS) and the program staff of CeNCOOS, who provided support for the collection and access to much of the data used in the thesis. Data used in the thesis was primarily collected by Prof. Karina Nielsen and her lab and Prof. John Largier. It is on their sweat and hard work that this study is built. Finally, I have to acknowledge the Moss Landing Marine Laboratories and the wonderful community here. The staff, students, and faculty are some of the most thoughtful and hardworking people I've had the pleasure of working with and I am grateful for the time I spent there.

INTRODUCTION

The coastal waters of the California Current Ecosystem have long been recognized for high levels of biological productivity, which supports commercially and ecologically valuable fisheries and robust coastal marine ecosystems (Carr, 2002, Pauly & Christensen, 1995). Eastern boundary currents, including the California Current Ecosystem, are responsible for more than 20% of the global fisheries catch while comprising of less than 1% of the global area of the oceans (FAO, 2002). In this system, productivity and ecosystem dynamics are largely coupled to seasonally persistent equatorward alongshore winds. Due to the rotation of the earth, alongshore winds result in offshore Ekman transport away from the coastal boundary and a subsequent upwelling of subsurface waters near the coast. The upwelling of subsurface waters along the coast (herein referred to as coastal upwelling) introduces bio-limiting macro and micro nutrients into depths where they are utilized by phytoplankton to fix carbon into organic carbon. Phytoplankton make up the base of the food web for both micro and macrozooplankton, including many benthic and pelagic organisms still in the larval stage (Cole and McGlade, 1998).

Canonically, coastal upwelling offers a framework for describing general trends in primary production in the California Current Ecosystem on a seasonal cycle across the west coast of the North America. On regional to local scales, chlorophyll concentration, which acts as a proxy for phytoplankton abundance, is often markedly decoupled from upwelling (Wieter et al., 2003). Complex spatial structure of the cross-shore wind field (Renault et al, 2016), mesoscale filaments and eddy structures, alongshore variability in relaxation cycles, and retention features from coastal bathymetry (Graham and Largier, 1997) and promontory features (Pickett and Franklin, 2006) all contribute to a spatial patchwork of both upwelling and biomass along the coast of Northern and Central California. Intermittency, or the cycling of winds from upwelling-favorable conditions to relaxed conditions, has also been shown to be an important and variable process linked to biological productivity at a regional scale (Menge and Menge, 2013).

In the nearshore environment, wave climate and beach hydrodynamics can greatly influence the abundance and community composition of nearshore phytoplankton (Morgan et al, 2018). The width of the surf zone, the beach interface (sandy vs rocky), as well as characteristics of the beach profile (reflective vs dissipative) have all been shown to be influential characteristics for phytoplankton abundance (Shanks et al, 2018).

The inner-self, an area defined by overlapping surface and bottom Ekman layers and that is offshore of the surf zone, is an important modulator of transport of plankton and nutrient rich upwelled water from the continental shelf break to the nearshore environment. Over the inner-shelf, alongshore surface stress becomes increasingly balanced by a bottom stress and less by Coriolis. One result of which is the reduction of cross-shore transport approaching the coastline (Dever et al 2006). Instead, onshore transport over the inner-shelf is largely controlled by cross-shelf wind and waves (Lentz et al., 2008). Surface gravity waves contribute to cross-shelf transport through a mechanism called Stokes drift, which is the result an incomplete closure of the orbital path of water as a wave propagates (Stokes G., 1847). Over the inner-shelf the magnitude of Stokes drift can be on the same order of magnitude as the Ekman transport, however unlike Ekman transport, Stokes drift velocities are not reduced while approaching the coastline and become an increasing important mechanism for onshore transport (Monismith & Fong, 2004). The depth-integrated, onshore transport from Stokes drift, called Stokes transport, Q_{stokes}, can be estimated using:

$$Q_{stokes} = \frac{gH_s^2}{16c}\cos\theta_w \qquad\qquad Eq.\ 1$$

Where g is gravitation acceleration, H_s is significant wave height, c is the phase speed of the wave, and θ_w is the direction of wave propagation, normal to the coastline. In order to conserve mass, Q_{stokes} must then be balanced by an offshore return flow, called undertow. The magnitude of Stokes drift decreases exponentially with depth, limiting the bulk of transport is to the upper meters from the ocean surface.

Despite the importance of wave-induced transport, few studies have examined how wave-induced transport over the inner-shelf affects nearshore biological processes. Instead, efforts have mostly focusing on surf-zone hydrodynamics (Morgan et al., 2018).

McPhee-Shaw et al (2011) observed that episodic increases in significant wave height squared, a proxy measurement for wave energy, co-occurred with peaks in intertidal chlorophyll-a timeseries at two different sites over 200 km apart in Northern California. They proposed a mechanism by which the wave climate, which is relatively uniform in this area, may be driving that variability, where increases in Stokes drift from larger waves can lead to a convergence of onshore transport trapping and concentrating phytoplankton into the nearshore. However, in the absence of ocean current observations, the mechanism remains untested.

This study focuses on understanding the physical mechanisms that couple offshore wind and offshore waves to nearshore phytoplankton variability by describing the statistical relationship between these variables. Using different multi-year *in situ* timeseries, a set of conditional averages are statistically described to characterize the changes in the ocean conditions associated with variability in chlorophyll-a at an intertidal site at Bodega Head in Northern California. Additionally, a reverse particle tracking model was developed to examine the origins and trajectories of water-masses that arrive in the nearshore during these periods, revealing how nearshore variability is links to the larger scale processes of the California Current Ecosystem.

BACKGROUND

STOKES DRIFT

As surface gravity waves propagate across the interface between the sea surface and the atmosphere, water particles are advected in an orbital path, progressing in the direction of propagation when at the peak of the wave and in the direction opposite of propagation when near the trough of the wave. The magnitude of the horizontal and vertical velocities during this orbit decrease with depth, one result of which is that the orbital path is not closed, resulting in a mass-transport velocity that is attributed to a second-order mean velocity (Figure 1a, 1b) (Stokes, 1847). Stokes drift ($\mathbf{u}_{St}$) can also be defined as the difference between the wave-average velocity while following a particle Lagrangian velocity ($\mathbf{u}_L$) and from a fixed frame of reference, Eulerian velocity($\mathbf{u}_E$)(Eq 1)

(Longuet-Higgins, 1969):

$$\mathbf{u}_{St} = \mathbf{u}_L - \mathbf{u}_E \qquad\qquad Eq.\ 2$$

As such, Stokes drift is not directly measured by typical Eulerian current measurements used to characterize inner-shelf and surf zone transport and instead must be calculated from *in situ* wave measurements, wave models (Webb and Fox-Kemper, 2011) or estimated from the wind field (McWilliams et al, 1999).

Using bulk wave parameters, which assumes a monochromatic wave, Stokes drift vectors are calculated as:

$$(u_{st}, v_{st}) = \frac{H_s^2 \omega}{16} \frac{\cosh\left(2k_p(z+h)\right)}{\sinh^2(k_p h)} k_p(\cos\theta, \sin\theta) \qquad Eq.\ 3$$

where H_s is the significant wave height, θ is the mean wave direction, h is the water depth, z is the vertical coordinate, k_p is the bulk wave number, and ω is the angular wave frequency. The wave dispersion relation defines the relationship between ω and k_p as $\omega^2 = gk_p \tanh(k_p h)$, where g is gravitational acceleration. For a monochromatic wave, the magnitude of Stokes drift decays exponentially with depth (Figure 1c), where at a depth of $z = L/4$ where L is the monochromatic wavelength, $\mathbf{u}_{St}$ is 4% of the surface value $\mathbf{u}_{St}$.

Bulk wave parameters are useful when bandwidth or computing resources are limited, however they do not inherently contain information about the spread of energy across the wave spectrum, nor the directional spread of the energy. The result is often an overestimation of the magnitude and depth distribution of Stokes drift (Kumar et al., 2017). Swell in Northern California is often generated remotely from large storm systems and may be opposed or non-parallel to locally generated wind-waves. To account for differences in the direction of wave energy, a directional wave spectrum, $\boldsymbol{S}_{\eta\eta}(\boldsymbol{f}, \boldsymbol{\theta})$, can be used in the estimation of Stokes drift using:

$$(u_{st}, v_{st}) = \int\limits_0^{2\pi} \int\limits_0^\infty \sigma k(\cos\theta, \sin\theta) S_{\eta\eta}(f, \theta) \cosh\frac{[2k(z+h)]}{\sinh^2(kh)} \, df d\theta \quad Eq.\ 4$$

where σ is the angular frequency and k is the wave number at each frequency band of the wave spectrum.

HIGH FREQUENCY RADAR

High-frequency radar (HFR) is used to synoptically map ocean surface currents in near-real time. Over the past 30 years, this technology has matured into a cornerstone for ocean observing networks and a vital tool in search and rescue operations, oil spill mitigation, maritime navigation, and other activities that require near real time surface current measurements (Paduan and Washburn, 2013). HFR has also been widely used in oceanographic research to describe physical patterns in surface currents such as upwelling surface current patterns (Paduan et al 2016), Lagrangian coherent structures (Shadden et al, 2009), modeling tides (Solabarrieta et al 2016), estimating wind and wave fields and tsunami detection (Grilli et al 2017). HFR has also been used, although to a lesser extent, in biological settings in fisheries managements, by modeling larval dispersion of important commercial fisheries (Roarty et al 2010), crustacean larval dispersion (Morgan et al 2009), and to examine patterns in phytoplankton distributions (Hernández-Carrasco et al 2018).

HFR operates by observing Doppler backscattered signals that result from Bragg scattering, the phenomenon of a certain band of radio waves scattering off of surface gravity waves in a predictable way. The difference between the expected theoretical backscatter signal and the observed Doppler shift in the Bragg peaks of the backscatter signal is interpreted as the radial surface current, or the motion of water towards or away from the HFR shore station (Paduan & Garber, 2007). The radial velocities represent a combined measurement of geostrophic and Ekman driven flow. The depth of the surface current measurement is dependent on the transmission frequency of the HFR and for a typical mid-range station of 10-12 MHz, as is used in this study, the measurement can be interpreted as an exponentially weighted average measurement of surface currents from the surface down to 1 meter (Röhrs et al., 2015). If multiple HFR shore stations overlap in coverage, total surface current vectors can be calculated from the independent radials (Paduan and Washburn, 2013). Depending on the configuration of the radar, the spatial resolution varies from 500 meters to 6 kilometers and can extend from 10 kilometers to 200 kilometers offshore.

While HFR surface current mapping has been widely utilized by global ocean observing systems, there is still some uncertainty within the literature as to exactly what types of velocities are represented in the measurements. Ardhuin et al (2009) suggest that HFR surface current measurements represent a quasi-Eulerian measurement, consisting of the Eulerian surface current and a portion of the Stokes drift, called the filtered Stokes drift. This filtered portion of Stokes drift is suggested to be related to the frequency of the instrument, which corresponds to the phase velocity of the Bragg waves measured calculate surface currents. Röhrs et al (2015), however, suggests that HFR surface currents are entirely Eulerian, as they are measurements of a fixed spatial region, and that a wave cannot, according to linear wave theory, be advected by its own mean drift velocity. This conclusion was supported through the comparison of HFR-derived surface current measurements with measurements from drifters and ADCPs with high vertical resolution near the surface. Given the complexities of this measurement and uncertainties surrounding it, this study will rely on what Röhrs et al (2015) empirically supported, an understanding of HFR derived surface currents as being entirely Eulerian, which ultimately puts more weight on influence of Stokes drift.

DATA AND METHODS

INTERTIDAL AND SHORE STATION WATER QUALITY

A WET Labs (Sea Bird Scientific, Bellevue, Washington) ECO FL fluorometer and Tidbit V2 temperature data logger was deployed annually, generally from March to September, in the intertidal (0-0.3 meters above MLLW) rocky shores at Bodega Head (38.318739 N, 123.074186 W) in Northern California (Figure 2b) by researchers from the Estuary and Ocean Science Center at San Francisco State University (https://www.cencoos.org/data/shore/intertidal/bodegahead). Quality controlled (QC) data was made available for download by the Central and Northern California Ocean Observing System (CeNCOOS) (Figure 3a). Data QC includes an out-of-water flag based on tidal heights and a sensor-fouled flag. Flagged data were disregarded. Salinity, temperature (Figure 3b), and chlorophyll-a time series, herein referred to as the shore-station, were retrieved from the Bodega Marine Laboratory's (BML) Bodega Ocean

Observing Node (BOON, http://boon.ucdavis.edu). An SBE 16+ Seacat (Sea Bird Scientific, Bellevue, Washington) was deployed to monitor conductivity and temperature of water drawn from Horseshoe Cove (38.31617 N, 123.0695 W) through a seawater intake system. Additionally, shores side wind speed and direction were also retrieved from BML BOON. Shore station chlorophyll-a was used, when available, to corroborate the presence of high chlorophyll as determined within the intertidal fluorescence record. Seawater temperature and chlorophyll timeseries were low-pass filtered using a Lanczos-cosine filter with a 40-hour cutoff (Thompson, R., 1987).

CHLOROPHYLL-A EVENT DETECTIONS AND CONDITIONAL AVERAGES

High-chlorophyll events were identified by calculating an annual threshold for each year as 1 standard deviation above the mean for that deployment (April through June). Events are therefore defined as intertidal chlorophyll values exceeded the annual threshold and are not within 40 hours of the previous event. Thresholds were calculated annually in order to avoid biasing event detection with interannual variability. Events were labelled at the peak amplitude (local maxima) of the chlorophyll-a. For each event, all data was collected up to 97 hours before the peak. Ninety-seven hours was chosen as being a long enough to capture the conditions before the event based on an analysis of intertidal chlorophyll-a autocorrelation which reveals that beyond a 20 to 38 hours lag, autocorrelation greatly decreased (Figure 6), therefore conditions greater than 40 hours before the peak as used to represent background or ambient conditions.

To preclude *in-situ* growth as the primary source of variability in chlorophyll, the rate of accumulation of chlorophyll-a was calculated for each event using Eq. 5 and doubling time using Eq. 6 where calculated for each event. Doubling time was calculated by fitting an exponential to intertidal chlorophyll conditional average ($f(chl) = 4.25 * e^{-.0837*t} + 0.381$) and used to calculated an accumulation rate and doubling time as:

$$\text{accumulation rate} = \frac{\ln\left(\frac{\text{chl}_{\text{peak}}}{\text{chl}_i}\right)}{t_i - t_{\text{peak}}} \qquad \textit{Eq. 5}$$

$$\textit{Eq. 6}$$

$$\text{doubling time} = \frac{\ln(2)}{\text{growth rate}}$$

where chl_i is the ambient intertidal chlorophyll value at 40 hour. To calculate the rate of change in intertidal chlorophyll-a, the time derivative of chlorophyll-a was calculated at each timestep for each event (Figure 4b).

WAVE AND METEOROLOGICAL RECORDS

Hourly directional wave spectral data was collected from National Data Buoy Center (NDBC) buoy 46013 (38.238 N 123.307 W, depth=123 meters) and Coastal Data Information Program (CDIP) wave riding buoy 029 (37.9499 N, 123.4717 W, depth=550 meters) (Figure 2a). Spectral wave data from CDIP 016 was preferentially used when available. CDIP 029 uses a Datawell Waverider MkIII buoy which is capable of resolving higher frequency bands in the wave spectrum than the larger 3-meter discus-type buoy used at NDBC 46013. A linear correlation of significant wave height measured from these two buoys reveals a strong correlation ($r^2 = 0.863$, $H_{s\,cdip} = H_{s\,NDBC} * 0.999 + 0.278$) Both the NDBC and CDIP sites are deep enough to ignore refraction due to interactions with bathymetry.

Directional wave spectra, $S_{\eta\eta}(f, \theta)$, are computed in the process of calculating the surface stokes drift velocities. $S_{\eta\eta}(f, \theta)$ can be written as the product of the energy spectra and the wave spreading function:

$$S_{\eta\eta}(f, \theta) = C_{11}(f)\, D(f, \theta) \qquad \textit{Eq. 7}$$

For NDBC archives the directional Fourier coefficients are used to construct a directional spreading function using:

$$D(f, \theta) = \frac{\frac{1}{2} + r_1 \cos(\theta - \theta_1) + r_2 \cos[2(\theta - \theta_2)]}{\pi} \qquad \textit{Eq. 8}$$

where r_1 and r_2 are directional Fourier coefficients, θ_1 is the mean wave direction, and θ_2 is the principal wave direction (Earle, M., 1996, O'Reilly et al., 1996). To calculate the directional spectrum from CDIP data, the coefficients of the directional Fourier series expansion are first derived from the cross-spectral transform parameters provided by CDIP (Earle et al., 1999). Finally, hourly surface Stokes drift vectors are calculated from $S_{\eta\eta}(f, \theta)$ using Eq (4). Routines for calculating directional wave spectra and surface Stokes drift used in this analysis are available at https://github.com/patcdaniel/SpectralStokes-equations in the Python computing language.

Hourly wind speed and direction was retrieved from NDBC 46013 for 97 hours preceding high chlorophyll-a events. The principal axis was determined for wind velocity from March through September for all available data from 2007 to 2012. The principal axis, 44 degrees counterclockwise to true North, approximates the angle of the coastline in Northern California and was used to define a new frame of reference where alongshore (poleward is positive) corresponds to the principal axis of the offshore wind and cross-shore (onshore is positive) corresponds to the axis orthogonal to the principal axis. Wind stress was calculated for offshore wind vectors using the Python airsea package (https://github.com/pyoceans, developed by Filipe Fernandes and Kyle Wilcox), using methods from Large and Pond (1981). Offshore sea surface temperature (SST) was collected hourly from the CDIP 029 waverider buoy. Bathymetry data are from the Coastal Relief Model (National Geophysical Data Center, 2003).

HIGH FREQUENCY RADAR DERIVED SURFACE CURRENTS

High Frequency Radar surface currents were aggregated from 2007 through 2012. Hourly surface current data from 2008 through 2011 was obtained with from the Coastal Observing Research and Development Center (CORDC) and gridded into netCDF4 files for each year. Surface currents for 2012 was retrieved from the HFRNet thredds data server (http://hfrnet-tds.ucsd.edu/thredds/catalog.html) as gridded netCDF4 files.

Ninety-seven hours of surface current data preceding high chlorophyll-a events, as described above, were aggregated for each identified event. Only surface current data

from grid points where greater than 90 percent of the data was available during the 97-hour record was used. Gaps in surface currents were filled first through linearly interpolating a grid point through time, then through a bilinear interpolation from surrounding data points. In order to fill gaps at the beginning and end of the surface current record, six hours of the surface current time series where added before and after the 97-hour timeseries and removes following linear interpolation.

Conditional Averages

The aggregated data from each event was combined into a conditional average of all of the identified events. Here the term 'conditional average' is used as a loose analog to what in probability theory would be described as the conditional expectation (Paduan et al. 2016). The conditional average is used here to capture an idealized state of the physical parameters (wind, currents, temperature, and wave fields) directly preceding and during rapid increases in intertidal chlorophyll. This is important as there were often conditions of large waves, but no intertidal chlorophyll, but seldom conditions of high chlorophyll but small to no waves (Figure 3a,b) making it difficult to decouple what conditions are driving increases in intertidal chlorophyll.

To calculate the conditional average, data were adjusted to the same timeseries using a linear interpolation between the nearest surrounding values. For all of the aggregated data for each parameter, a Shapiro-Wilk tests were performed at 13 hours before the peak in chlorophyll and 48 hours before the peak. Thirteen hours before the peak was chosen to represent a condition during the event, as this was the time of the maximum time derivative of median conditional average of intertidal chlorophyll (Figure 4b). Conversely, 48 hours before the peak was chosen as a time to represent the conditions before any increases in intertidal chlorophyll was observed. Where the Shapiro-Wilk test rejected the null hypothesis that the data were drawn from a normal distribution (p=0.05), data from that parameter was treated as non-parametric and median values are reported as the average (Table 1), otherwise the mean values were used as the average.

REVERSE PARTICLE TRACKING MODEL

Particle tracking is a way to estimate trajectories of water masses by calculating the velocity of a virtual particle and advecting it to the new position at each timestep. This process is repeated until certain conditions are met, like the particle has left the model domain or a certain amount of time has elapsed. Particle tracking models can also be run in reverse to estimate where a particle was transported from. Here, reverse particle trajectories were calculated using a reverse Lagrangian particle tracking model that is forced by hourly HFR-derived surface current data. Particle positions were solved at each timestep using a 4th order Runge-Kutta scheme, with a 15-minute timestep. A fixed timestep of 15 minutes was determined to satisfy the requirement that no particle is advected greater than one quarter of the length of the HFR spatial grid (2km) in a single timestep. During model development, the use of a variable timestep was evaluated and determined to produced similar results to the fixed timestep. Starting at the time of each high chlorophyll-a event, virtual particles were advected backwards in time until they left the domain of the model or 96 hours before the time of the event. Particle vector velocities were estimated using a bilinear interpolation scheme from the surrounding nearest HFR surface current grid nodes. When particles were advected out of the model domain, which is determined by the quality of the HFR surface current map at time of interest, they were removed from the model.

To calculate each trajectory, 25 particles were seeded within a circle with a radius of 500 meters. The center of circle was set at 38.29 N, 123.11 W approximately 4 kilometers offshore from the intertidal site. This position was chosen due to the configuration of the HFR in the area, which does not measure surface currents within 2km of the coastline. Positions for all particles were calculated at each timestep. The mean position at each timestep was calculated as the center of a centroid draw around all of the particles.

To examine the effect of Stokes drift on reverse particle trajectories, surface Stokes drift estimates were added to the HFR derived surface currents to give a total velocity. For each event a particle trajectory as calculated using both the total velocity (HFR + surface Stokes) and HFR-only surface currents. Bottom depth at the mean particle position for each timestep was estimated though a bilinear interpolation of the

Coastal Relief Model (NOAA National Centers for Environmental Information, U.S. Coastal Relief Model, Retrieved: July, 2018, http://www.ngdc.noaa.gov/mgg/coastal/crm.html). Position, bottom depth, and the timestamp we recorded for 31 events particle trajectories for statistical analysis. The spread between trajectories forced with Stokes drift and those forced without Stokes drift was also calculated as the distance between the mean positions at each timestep and was calculated using Vincentry's formula from the geopy package (https://github.com/geopy/geopy). All distances are calculated to the WGS-84 refence datum.

MOPS NEARSHORE WAVE MODEL

To estimate nearshore wave conditions and surface Stokes drift, the Monitoring and Prediction System (MOPS) model produced by CDIP was used (O'Reilly et al., 2016). The MOPS model estimates the nearshore wave energy at the 15-meter isobath by assuming a linear propagation of the of spectra as measured by in situ offshore wave buoys. Model validation from various sites across California showed the model has relatively high skill in areas with where bathymetric features are less complex and poorer skill in areas such as channels or sheltered coastlines. Because of the largely open coastline in the area of this study and isobaths over the shelf being generally normal to the coastline, the MOPS model was considered an adequate proximity for nearshore wave conditions in the absence of in situ measurements. Directional wave spectra were calculated in the same manner as they were calculated for from the in situ offshore data. Surface Stokes velocities were calculated from directional wave spectra using the same methods outlined for the *in-situ* wave measurements. One source of error in this calculation comes from the MOPS model not being capable of modeling the wind-wave portion of the wave spectra, which is instead, dependent on local conditions.

RESULTS

INTERTIDAL CHLOROPHYLL-A EVENTS

From 2008 to 2012, 41 independent high chlorophyll-a events were identified between the months of March and October. The annual distribution of identified events was constant with a minimum of 7 identified events each year and a mean of 8.2 per year, with no apparent annual trend in the number of events. Events were most common between March and June, which corresponded to a well-established upwelling season (April to June) in Northern California (García-Reyes & Largier, 2011), but were also observed as late as October. When available (n=24), an independent chlorophyll-a timeseries from the nearby seawater intake of BML, located in Horseshoe Cove was used to corroborate the response time and phase of the intertidal timeseries. A linear regression between intertidal chlorophyll and tidally-filtered shore station chlorophyll up to 96 hours before the intertidal chlorophyll-a peak reveals an strong correlation ($r^2 = 0.823, p < 0.01$), suggesting that the intertidal chlorophyll response is not an artifact of the intertidal fluorometer location, and lending confidence to the accuracy of relative changes in the fluorescence signal.

The temporal scale of decorrelation for intertidal chlorophyll was determined using an autocorrelation function of intertidal chlorophyll-a timeseries for each year (Figure 5). In all years, the autocorrelation decreased below 0.5 between a lag of 24 to 40 hours. A similar result was found by Wilcoxon sign-ranked test between each hour of the aggregated intertidal chlorophyll-a event dataset. After 40 hours, the correlation value of chlorophyll-a at the peak was below 0.5 and no longer significant (p=0.05) with chlorophyll-a greater than 40 hours before the peak, suggesting that intertidal chlorophyll accumulation occurs in two stages, first a slow increase in from 40 to 24 hours before the peak and faster increase between 24 to the peak.

A similar analysis was ran using the tidally-filtered intertidal temperature timeseries, where the auto correlation fell below 0.5 at a lag of 150-175 hours for all year, suggesting that temperature is controlled largely by processes that are on the scale of weather features. Temporal changes in temperature appear to occur on a different timescale from intertidal chlorophyll.

Accumulation rates of the intertidal chlorophyll conditional average were calculated to be 0.84 µg L-1 per day which corresponds to a doubling rate of 19 hours. The maximum rate of change occurred at 13 hours before the peak.

PHYSICAL CONDITIONS

In the time preceding the conditionally-averaged chlorophyll-a events, offshore wind stress is predominantly alongshore and equatorward (Figure 4c). Wind stress began to increase in magnitude 40 hours before the peak, plateauing at 7 hours before the peak. At 3 hours be the peak in intertidal chlorophyll, wind stress begins to relax. Relaxation of alongshore wind stress was present preceding most events (n=26) and a wind reversal pattern was seen in several events, all observed in 2012 (n=5). An analysis of autocorrelation of alongshore wind stress during each event shows a similar pattern, where wind stress at the peak of chlorophyll and the preceding 30 hours was well correlated, while there is a strong decrease in correlation with wind stress beyond 40 hours before the peak (Figure 6a). A similar pattern was occurred with offshore significant wave height (Figure 4d). Further, there was no statistically significant change in either the dominant wave period, or the mean wave direction over the course of the conditional average. Wind direction and wave mean direction (Figure 8a,b) are both strongly aligned with the alongshore principal axis, roughly parallel to the shoreline south of Point Arena. These wind conditions suggest that alongshore winds were generating the waves, as opposed to longer period swells, which are generally generated from episodic remote storms. Alongshore wind stress and significant wave height were also negatively correlated (Figure 8c). A cross-correlation between the magnitude of offshore wind stress and the wave height shows that significant wave height at 20 hours before the peak is significantly correlated to wind stress from 40 to 10 hours before the peak, which can be interpreted as the significant wave height is increasing as the ramping up winds continue to impart energy to the waves (Figure 9).

Intertidal chlorophyll-a signal peaked 3 to 5 hours after these both wind stress and significant wave height began to relax (or at least were no longer monotonically increasing). This may be attributed to a lag in offshore measurements reflecting nearshore conditions. When comparing significant wave height measured from two different buoys (CDIP 029 and NDBC 46013) located approximately 45 miles apart (Figure 2a), there is little difference in pattern of significant wave height, suggesting that the offshore wave climate is generally uniform in this area.

TEMPERATURE

The conditional average of intertidal temperatures did not exhibit any statistically significant change. In the Bodega Head area, seawater temperature and sea water salinity are strong tracers for the origins of the water mass (Paquin, M.S. Thesis, 2012), however no coherent pattern was observed. In order to account for some of the seasonal and interannual variability in temperature, relative changes in temperature were examined by removing the mean of each temperature timeseries in each event, revealing what appeared to be a slight decrease in the mean intertidal temperature residual (0.3 °C) starting at 20 hours before peak to 0 hours before peak. However, a t-test revealed no statistical significance between the temperatures. In several cases (n=4) intertidal temperatures did increase with chlorophyll. This general lack of a pattern in the change in temperature was also supported by similar patterns that were observed in the BML shore station temperature timeseries.

STOKES DRIFT AND SURFACE CURRENTS

Estimations of surface Stokes drift, $\mathbf{u}_{ss}$, showed a strong correlation with the wind stress (Figure 5). When rotated into an alongshore-onshore coordinate plane based on the principal axis of alongshore wind stress, $\mathbf{u}_{ss}$ was predominately in an equatorward alongshore direction. This is unsurprising as both the direction of wind and wave propagating were predominately negative in the alongshore direction (Figure 7ab) . The magnitude of Stokes drift nearing the event peak was up to half of the magnitude of the alongshore transport as measured from 8km by 8km spatial mean taken from nearshore, mid-shelf, and offshore (Figure 2a, Figure 3 fg). In the case of the nearshore surface current average, Stokes drift velocities varied between 25 to 55 percent of the surface current values measured by the HFR.

Surface Stokes drift was also calculated in the nearshore using the CDIP MOPS spectral refraction model (Figure 3e). Surface Stokes drift was primarily in the onshore vector, demonstrating wave refraction. The relative changes in magnitude of offshore alongshore drift and nearshore onshore drift were similar. This data does not reflect effects of local wind on the wave spectrum as they propagate from the offshore, which

could potentially have an important effect on Stokes drift. To assess this effect, shore-based wind records were assessed for large disagreements with offshore alongshore wind stress and generally agreed with offshore wind stress ($r^2 = 0.634$, $p < 0.01$, $\tau_{v\,offshore} = \tau_{v\,shore} * 2.86 - 0.046$).

PARTICLE TRACKING

High Frequency Radar (HFR) has been widely used for particle trajectory modeling, from validation measurements alongside drifters (Kaplan & Largier, 2006, Solabarrieta et al 2016) to describing oceanographic features (Shadden et al 2009). Virtual particle tracking was used to show the offshore origins of particles (i.e. water masses) that arrive in the nearshore, the influence of including Stokes drift on particle trajectory, and as well as to examine some of the spatial structure associated with offshore transport in this region. The particle trajectories were estimated for 34 events from HFR-derived surface currents and HFR-derived surface currents with a calculated *in situ* surface Stokes drift term added. The majority of particle trajectories originating from the north (n=26). Particles often exited the domain of the HFR within 12-48 hours, limiting information about the originating water masses North of 38.4° N. Trajectories were categorized based on origins of the surface waters and whether the origin was to the north (Figure 12a) or south (Figure 12b) of the seed position.

Mean trajectory bottom depth values (Figure 11c) for each position along the trajectory were collected for at each timestep. Consistent with most water masses originating from the north, trajectories tended to follow along isobaths. There was not a statistical difference between the bottom depths of trajectories forced with or without Stokes drift. The average rate of spread between trajectories forced with and without Stokes drift was 0.22 km/hr (std: 0.047 km/hr). This generally linear increase in spread and the low standard deviation suggests that the differences in the rates between the trajectories with and without Stokes drift were relatively constant.

Particle trajectories were estimated for 34 events by seeding particles nearshore at the time of peak intertidal chlorophyll-a and back calculating particle position until the particle leaves the model domain or 48 hours passes. Nearly all of the particle trajectories showed a pattern of onshore transport leading up to the peak in nearshore chlorophyll-a.

The vast majority of these particles (n=26) originated from northwest of Bodega Head, often exiting the model domain within 12 to 24 hours. The bottom depth at each particle trajectory timestep was interpolated from the particle position from a global bathymetry model (figure 12c). The results show a slight trend in the mean towards deeper waters, although often the model runs were too short to resolve completely. The mean difference between offshore sea water temperature and intertidal temperature was approximately 0.75 degree Celsius warmer in the intertidal for these events.

DISCUSSION

NEARSHORE CHLOROPHYLL VARIABILITY

The episodic, high-chlorophyll events observed in the intertidal were well correlated with both increases in offshore significant wave height and alongshore wind stress. The seasonal distribution of these events mirrors increases in primary productivity related to the upwelling season in the California Current Ecosystem where the most events occurred between the months of April through. Intertidal phytoplankton abundance increases (0.84 μg L-1 per day) on scales similar to those described in *in situ* growth experiments (0.59 and 0.67 μg L-1 per day in oceanic and coastal waters, respectively) (Calbert and Landry, 2004). However, phytoplankton are not a conserved tracers, meaning they are subject to grazing and advection, in addition to growth (Shanks et al 2018) and what is measured in the intertidal should be thought of as the accumulation rate or the sum of growth, mortality from grazing and senescence, and advection. In the absence of data to quantify these terms, values from literature can be used to estimate the relative contribution of both growth and advection for these events. A meta-analysis of dilution experiments by Calbet and Landry (2004) provides rate of mortality from microzooplankton grazing for different ocean zones. The mortality rate of microzooplankton grazing on phytoplankton in coastal oceans was estimated to be 0.40 ± 0.04 μg L-1 per day. Subtracting microzooplankton mortality rates from the accumulation rate, the growth + advection rate is 1.24 μg L-1 per day. Based on the average growth reates reported by Calbert and Landry, the advection term would account for 0.57 μg L-1 per day, nearly matching growth. Additionally, microzooplankton grazing only represents

one form of phytoplankton mortality in the intertidal, so these values are ignoring the effects of intertidal filter feeders. This analysis suggests provides strong evidence that growth alone cannot account for the rapid increases in intertidal chlorophyll and instead it is important to considering both growth and accumulation. This consideration motivates the need to understand how Stokes drift and spatial variability in the surface currents can lead to these high chlorophyll events.

WIND AND WAVE VARIABILITY

Alongshore wind stress and significant wave height were both correlation with intertidal chlorophyll, understanding the linkage mechanism between these two physical drivers can be difficult to parse. Wind-forced Ekman transport from increased equatorward wind stress would characteristically result in the surface transport of waters offshore. These patterns were not directly observed by surface currents measured with HFR (Figure 4fg), instead surface currents were coherent with the direction of offshore wind stress. Alongshore wind stress began to increase around 40 hours before peak chlorophyll was observed. Significant wave height increased at a similar time scale to winds alongshore wind stress at 40 hours before the peak intertidal chlorophyll. Offshore alongshore wind stress and offshore significant wave height were significantly correlated (r-squared: 0.91, p <0.01) and both highly coherent in the alongshore direction (135° clockwise from north). This correlation implies that increases in wave energy are generated locally offshore from the wind, as opposed to swell generated from remote storms. An increase in wave energy imparted by wind is also reflected by increases in surface Stokes drift (Figure 7a), where the magnitude of wind stress was correlated (r-squared: 0.93, p < 0.01) with the magnitude of surface Stokes drift.

Recent research suggests that Stokes drift is very sensitive the effects of local winds (at frequencies in the wave energy spectra above 0.35 Hz) and highly correlated with wind direction (Clarke and Van Gorder, 2018). In particular using bulk parameters to estimate Stokes drift or Stokes transport (Equations 3 and 1, respectively) can lead to an over- or underestimation of the magnitude, direction, and depth distribution of Stokes drift and transport. As such, the increase in offshore surface Stokes drift during these events can be interpreted as the transfer of energy from wind stress into the wave spectrum, the result of which is an increase in magnitude of surface Stokes drift.

ESTIMATING NEARSHORE STOKES DRIFT

Surface Stokes drift calculated using the MOPS model were similar in magnitude and time scale as surface Stokes drift calculations made from offshore (Figure 4e). At the 20-meter isobath, about 650 meters from the coast, Stokes drift was almost entirely refracted into the onshore vector (Figure 4e, dashed lines), illustrating that using only the onshore vector (Equation 1) of the mean wave direction may not accurately represent conditions in the nearshore. Stokes drift estimates were larger than the nearshore surface cross-shelf velocities measured from HFR (Figure 2f) and on the same order of magnitude as the strong alongshore currents that form the coastal boundary layer in this region (Nickols, et al 2013). The magnitude of the nearshore Stokes drift is consistently smaller than the offshore Stokes drift. This is possibly explained by the narrower bandwidth of the MOPS model, which cannot predict local wind conditions. Another reasonable explanation would be a loss of energy due to bottom friction as the waves propagate to shallower depths. Both of these scenarios may be worth investigating closer, however the relative changes in surface Stokes drift between offshore and onshore are consistent.

PARTICLE TRACKING AND WATER MASS ORIGINS

The particle tracking model revealed most of the water masses preceding periods of high intertidal chlorophyll originated from the north (Figure 12a). This result aligns with previous studies which describe flow patterns where water originates from the Point Arena upwelling center and is advected south through persistent coastal jets (Halle and Largier, 2011).

Recalling that wind and waves are generally well aligned in direction, as Stokes drift seemed to reinforce surface current velocities. Given the high coherence between wind stress and surface currents in this area (Kaplan and Largier, 2006), it is not surprising that adding Stokes drift, which is heavily influenced by wind stress (Ardhuin et al, 2009, Kumar et al, 2017) may not be a large influence on particle origins in the offshore. This may be particularly true when the wave climate is also largely coupled to local wind conditions, as opposed to remotely generated swells, where waves propagating

oblique or opposite to the wind direction. In other locations, where tidal forcing is a dominant mode of surface currents, such as the mouth of the San Francisco Bay, including Stokes drift may yield vastly different results. Here, the results were also limited by seeding the model near the northern boundary of the model domain, which often resulted in the particles being advected out of the model soon after being released. Using a courser resolution (6 kilometers) HFR surface currents dataset was explored, however concerns over the model sensitivity to subscale processes precluded its use.

For the 8 events where the water masses did not originate from the north (Figure 12b), including surface Stokes drift resulted in a greater spread from the particles forced only by HFR surface currents. The greater spread can be attributed to surface currents and surface Stokes drift being in different directions, as well as the particles simply remaining in the domain of the model longer. The model also assumes a spatially uniform offshore wave climate, which seems reasonable, given the high correlation of different offshore wave measurements (Figure 4d) and that model domain is relatively unhindered by complex bathymetry or coastline features.

CONCLUSION

Nearshore phytoplankton dynamics are undoubtingly complex and highly coupled to physical processes. As such, it is important consider many different temporal and spatial scales and how they may be linked. Here, it has been shown that under specific set of conditions, ie an increased in alongshore wind stress and significant wave height, wave-induced transport, Stokes drift, theses physical drivers can influence nearshore phytoplankton variability by providing a mechanism to transport and accumulate phytoplankton into the nearshore.

These high chlorophyll events underscore the challenges of studying ephemeral processes, as a series of conditions seem to be required for phytoplankton to accumulate in the nearshore. Coastal upwelling needs to provide the basic ingredients for *in situ* phytoplankton growth, followed by coastal jets and southward surface currents to advect the upwelled waters to the south off of the Bodega Head. Finally, Stokes drift, induced by large waves that have bent towards the coast and are reinforced by winds along the way,

will provide a mechanism to transport phytoplankton near the surface through the coastal boundary layer over the inner-shelf and up against the coastline. The persistent onshore surface transport creates a convergence zone by which slightly buoyant phytoplankton are trapped and accumulate rapidly. Finally, when the waves and winds begin to reside the convergence zones diminish and phytoplankton abundance rapid subsides.

This transport and accumulation mechanism as first proposed by McPhee-Shaw et al (2011) still remains to be empirically tested. A preliminary 2D ROMS model forced using the physical state described by the conditional average was able to resolve both onshore convergence and an offshore Ekman-driven flow underneath the onshore surface flow (T. Connolly, unpublished). This type of model could be further developed to test different physical conditions as well different types of tracers. Additionally, deploying a cross-shelf transect of wave resolving ADCPs over the inner-shelf could provide direct observations of onshore convergence through Stokes drift.

This project has also willfully ignored the disciplines of both phytoplankton ecology and physiology. It has been convenient to consider phytoplankton as nearly passive fluorescent particles but understanding how physical conditions change the behavior and diversity of different phytoplankton will certainly provide important insight. A recent study in the Mediterranean Sea was able to track how nearshore phytoplankton regimes shift throughout the year using a similar type of particle tracking model to the one used here (Cianelli et al, 2017).

In the past two decades the understanding of inner-shelf dynamics has greatly improved and the importance of considering wave-induced processes when working in the nearshore environment has been well established (Monismith & Fong, 2004). Yet, few studies outside of nearshore and intertidal processes outside of physical oceanography consider the effects of Stokes drift and other wave-induced interactions. Just the same, few of the large inner-shelf experiments have strong considerations for the biological processes. This study has demonstrated that it was not uncommon for surface Stokes drift velocities to be on the same order of magnitude as more typically considered Eulerian velocities in the region (Nickols et al 2013), underscoring the importance of their consideration and that in order to better understanding biophysical interaction within the nearshore environment, it is imperative to consider the effects of these processes.

It was also important to demonstrate the use of spectra wave measurement for calculating Stokes drift. The use of bulk parameters such as significant wave height and average wave period to calculate Stokes drift may lead to errors in estimating the magnitude and depth distribution of Stokes drift (Tamura et al 2012). However, due to the high coherence between the direction of offshore wind stress and offshore waves as captured during these events, minimal directional spreading was observed. Further, because dominant wave periods were, by and large, shorter than remotely generated swell (< 10 seconds), it stands that the bulk parameters used to initially estimate Stokes drift do in fact produce reasonable results. However, given progress in availability of two-dimensional spectral wave data both from modeling outputs and *in situ* measurements, using these more conservative techniques for estimating the magnitude, direction, and depth distribution of Stokes drift should be the new standard.

The scale of variability considered here is one often aliased by satellite remote sensing, where the spatial resolution is often too course or not resolved near the coastline and the temporal resolution is greatly diminished by cloud cover and satellite orbital paths. For these reasons, *in situ* ocean observing efforts are still vital for filling in the gaps of where satellite remote sensing cannot resolve. As the quality, coverage, and accessibility of ocean observing efforts continues to improve, so will our understanding of these important biological and physical coupled processes (Cianelli et al, 2017). This study utilizes several ocean observing datasets and the statistical strength that comes with half a decade of data. These types of datasets, which are made openly available through national ocean observing efforts such as NOAA's Integrated Ocean Observing System and NSF's Ocean Observing Initiative make it possible and much easier to take a multidisciplinary approach to marine science, utilizing tools from different disciplines to find novel ways to answer questions.
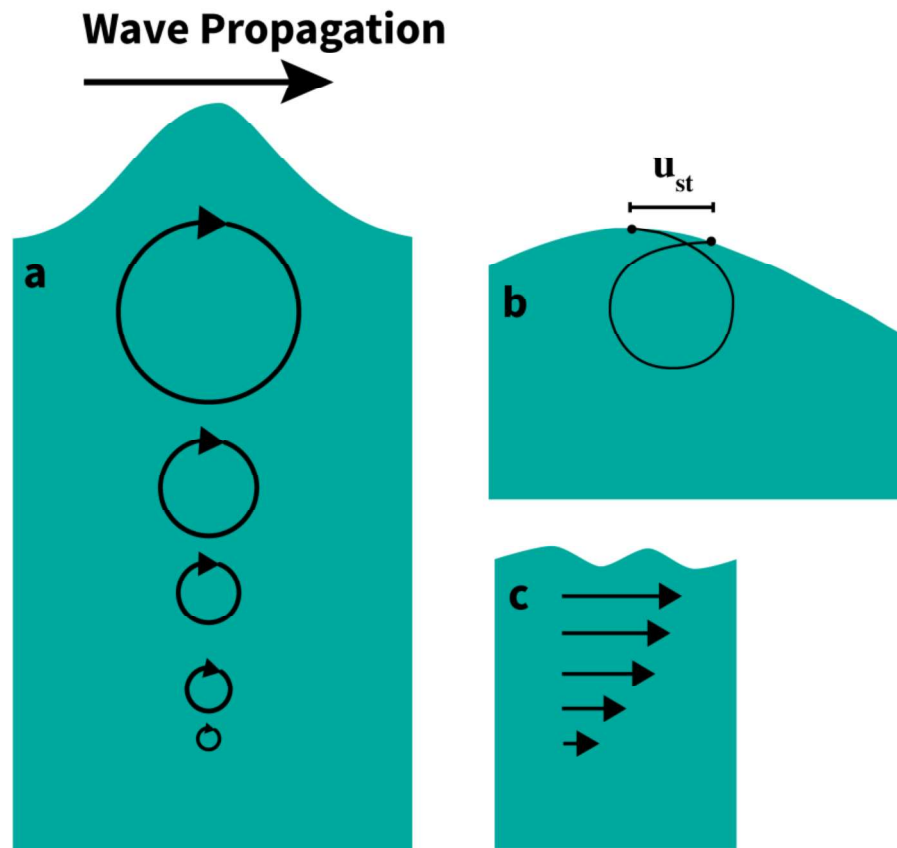
Figure 1. (a) For idealized waves (Gerstner waves) the orbital path that a water particle makes is a closed circle that decreases exponentially with depth. **(b)** Stokes drift is a result of the horizontal velocities of a water particle orbital path being slightly larger near the top of the orbit in the direction of wave propagation then in the bottom of the orbit, resulting in a slight movement in the direction of the wave propagation. **(c)** The magnitude of Stokes drift decays exponentially as a function of the wavelength of the waves.
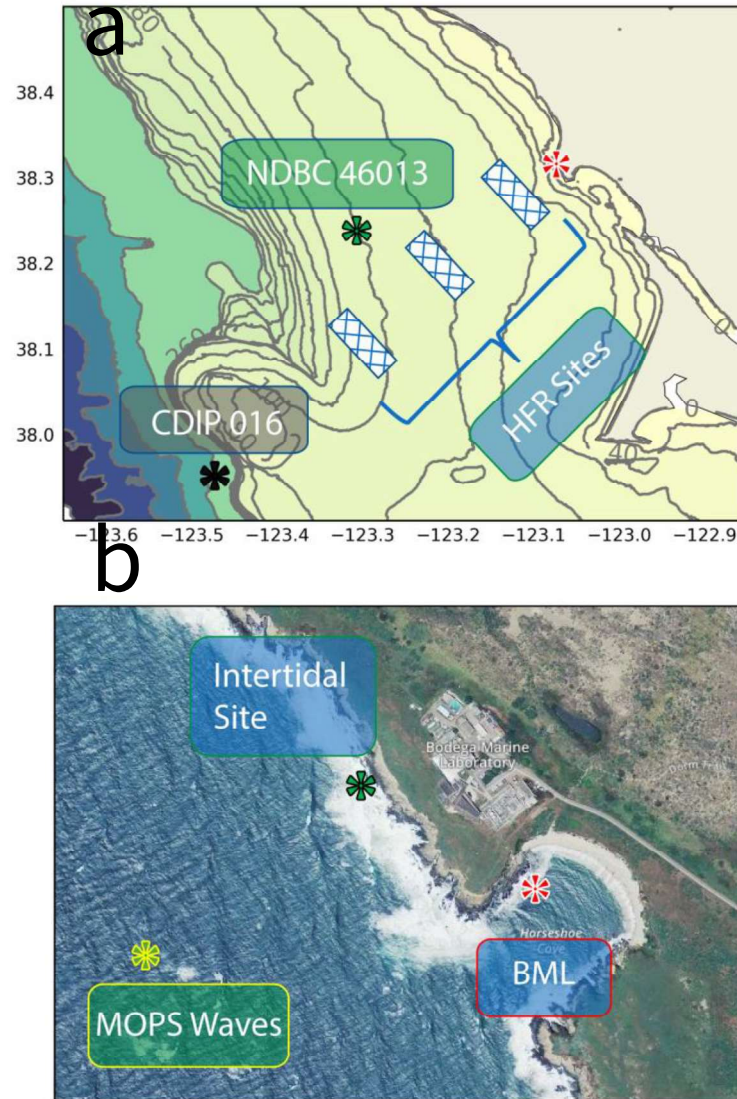
Figure 2. Study map of the Bodega Bay region in Northern California. **(a)** The NDBC 46013 buoy (green asterisk), CDIP 029 buoy (black asterisk), HFR radar sites used for timeseries analysis of surface currents are shown in the blue hatched boxes. Red asterisk corresponds to location of inset (**b**). **(b)** Showing the general location of the intertidal fluorometer deployments (green asterisk), the MOPS nearshore wave model node (green and yellow asterisk), and the Bodega Marine Laboratory shore station intake (red asterisk)
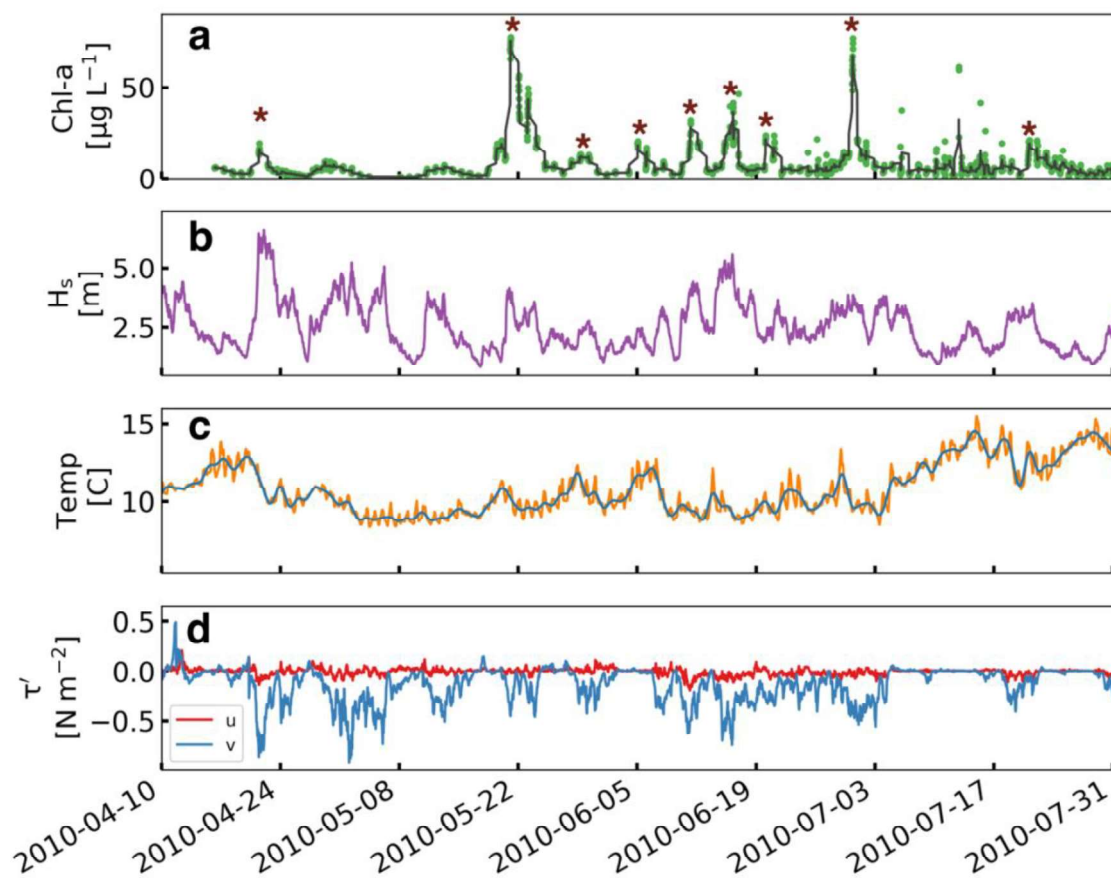
Figure 3. (a) Intertidal chlorophyll-a timeseries with a rolling hamming window (black line). Maroon asterisks denote "events" that are aggregated to form conditional average. **(b)** Significant wave height as measured from Bodega Bay NDBC buoy (#46013). **(c)** Intertidal temperature (orange line) and temperature after a 40-hour lanczos low-pass filter has been applied (blue line). **(d)**. Offshore wind stress vectors from the Bodega Bay NDBC buoy (#46013). Data were rotated along to the principal axis (-44 degrees from true North), where u is the cross-shore component (onshore is positive) and v is the alongshore component (poleward is positive).
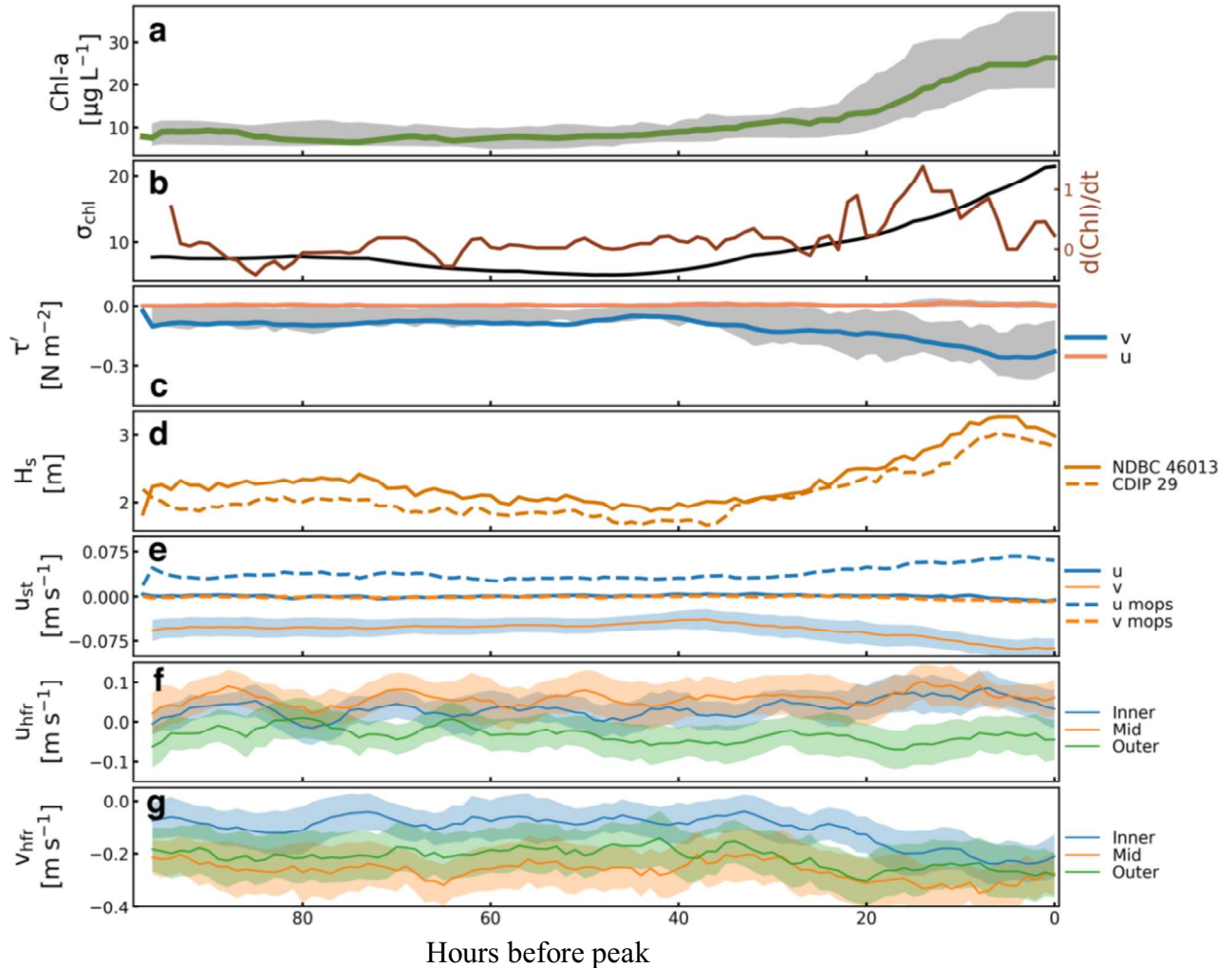
Figure 4. Conditional average timeseries for 41 nearshore high chlorophyll-a [units: $\mu g\ L^{-1}$] events that occurred from 2008-2012. **(a)** Median intertidal chlorophyll-a (solid green line) timeseries (grey shading, 95% confidence intervals) and median shore station chlorophyll-a timeseries (dashed green line) (n=22). **(b)**. Standard deviation of intertidal chlorophyll-a (solid black line) and time derivative (rate) of intertidal median chlorophyll-a (solid red line). **(c)** Median wind stress [units: Pa] vectors rotated to the principal axis (44 degrees counter clockwise from north) measured by NDBC buoy 46013 (38.238° N, 123.307° W). Alongshore vector (blue solid line) is positive in the poleward direction, onshore vector (solid orange line) is positive to the eastward direction. **(d)** Median significant wave height [units: m] from NDBC buoy 46013 (solid orange line) and CDIP buoy 029 (37.950° N 123.472° W)
(dashed orange line). **(e)** Median surface stokes drift velocities [units: m s^{-1}]. Offshore onshore vector, u, (solid blue line) and offshore alongshore, v, (solid orange line)

calculated from directional wave spectra of NDBC buoy 46013 and CDIP buoy 029. Nearshore onshore vector, u mops, (dashed blue line) and nearshore alongshore vector, v mops, (dashed orange line) of the surface stokes drift, computed from the alongshore MOPS wave spectra model at 38.3139° N, -123.0788° W, z=20 meters). **(f)** Onshore and **(g)** Alongshore vectors of High Frequency Radar (HFR) derived surface currents at three sites (shading indicates 95% interval): inner (blue line), mid (orange line) and outer (green line).
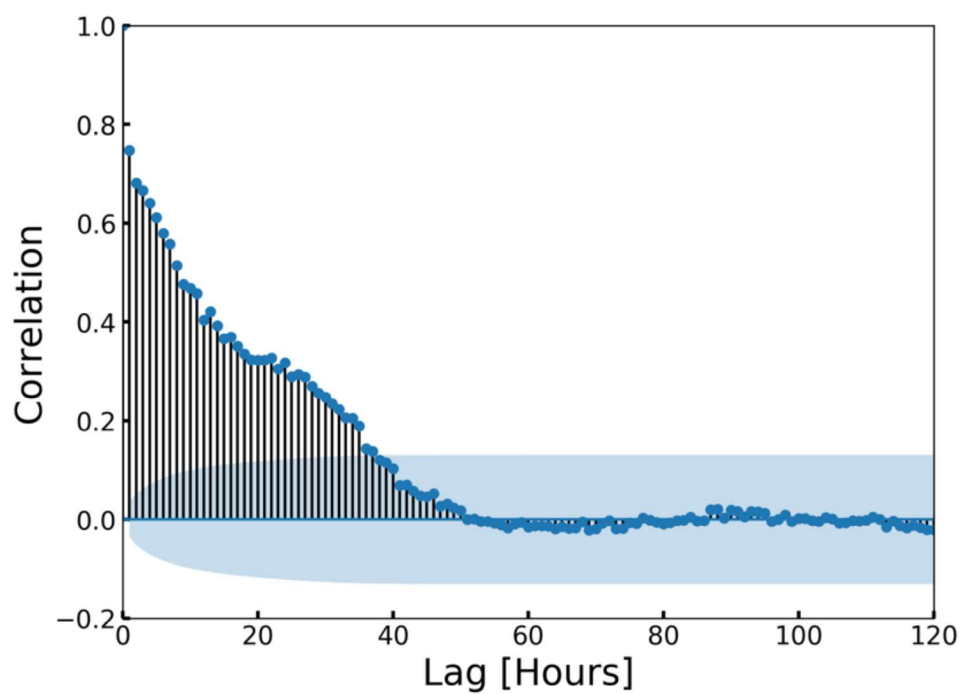
Figure 5. Figure 3. Autocorrelation of intertidal chlorophyll-a timeseries for the year 2010. Light blue cone indicates 95% confidence interval in the correlation.
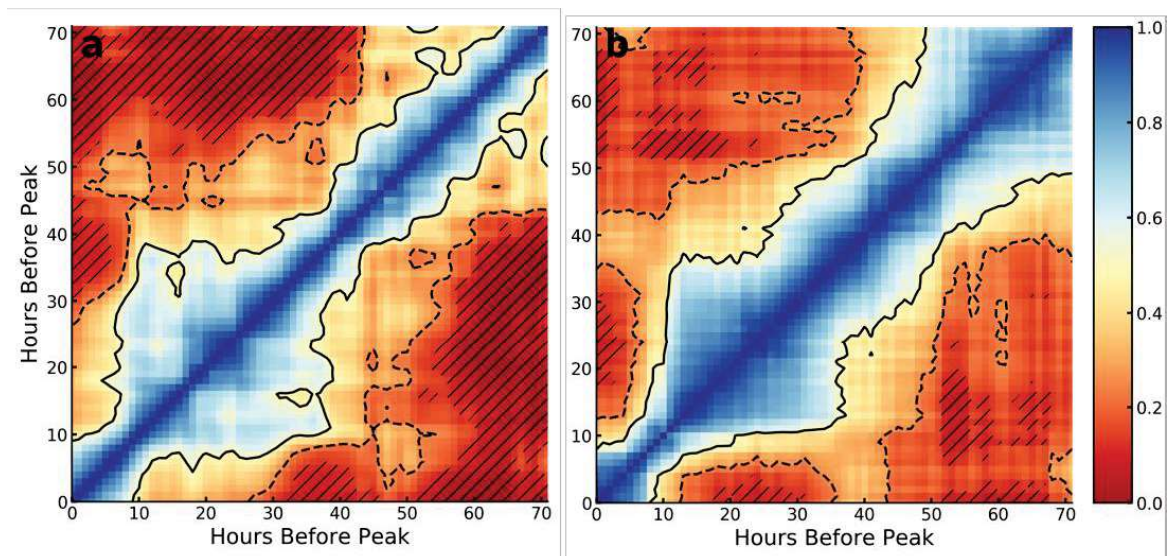
Figure 6. Autocorrelation of **(a)** offshore alongshore wind stress and **(b)** offshore significant wave height. Contour lines denotes the spearman correlations coefficients (solid 0.5, dashed 0.25). Hatched areas denote areas where correlation was not significant (p > 0.05).
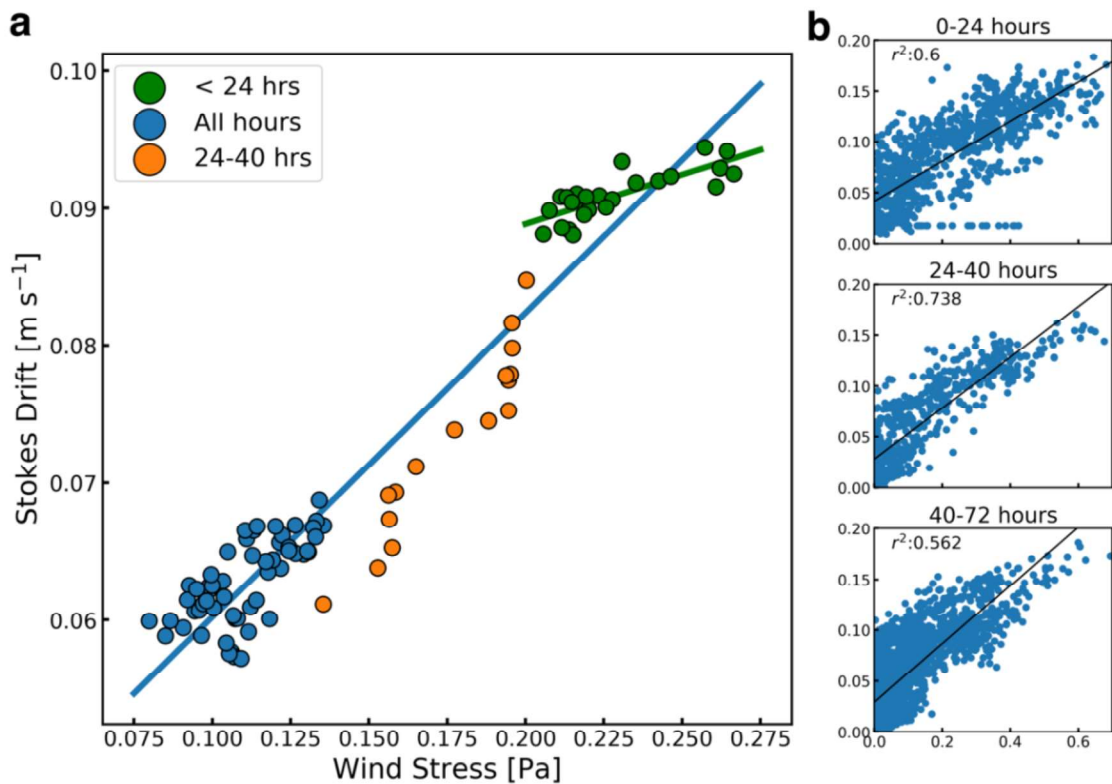
Figure 7. (a) Linear regression of conditional averages of surface Stokes drift and wind stress for all hours (blue line, r^2=.93, $p < 0.01$) and within 24 hours of peak event (green line, r^2=.64, $p < 0.01$). Data colors correspond to the different time ranges; green: <24hrs, orange: 24-40 hours, blue: > 40 hours from peak. **(b)** Linear regressions of Stokes drift against wind stress for all events for each of the same time periods.
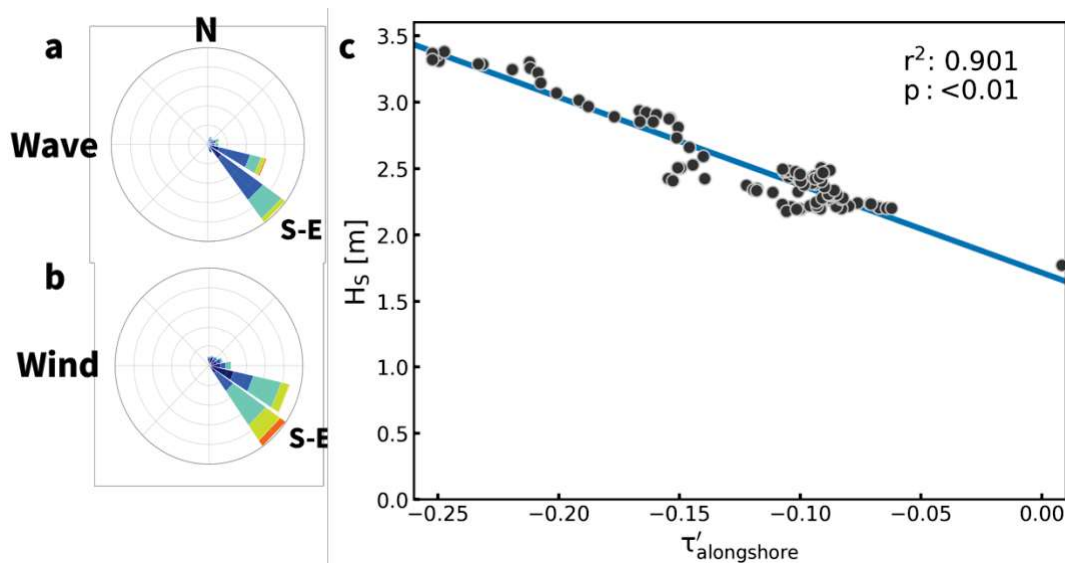
Figure 8. (a, b) Wind rose plot for all events (n=33) showing wave direction **(a)** and wind direction **(b)**. Colors correspond to bins of different wave height (a) and wind speed (b). High coherence in the cardinal direction of South East (S-E) of the wind and wave climate of the 96 hours preceding the peak in intertidal chlorophyll. **(c)** A linear regression between the conditional averages of alongshore wind stress [units: Pa] and significant wave height [units: meters] ($r^2 = 0.901$, $p < 0.01$) shows a strong negative correlation.
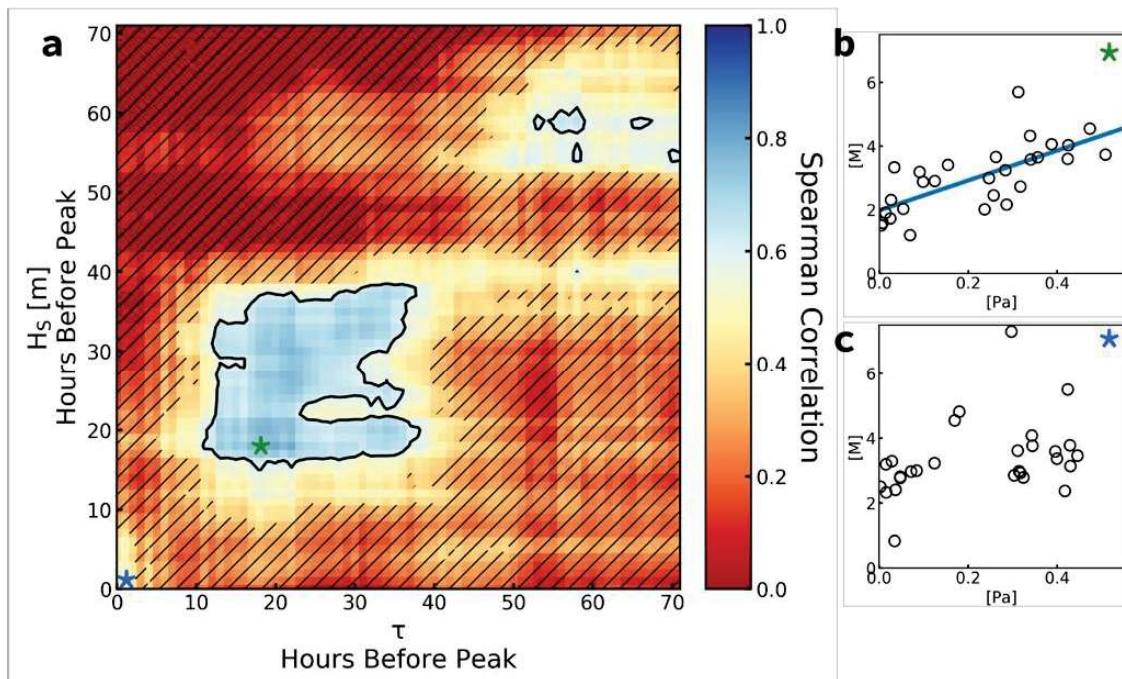
Figure 9. (a) Cross correlation with offshore significant wave height and offshore wind stress magnitude, determined using a Spearman rank-order correlation. Contour denotes statistical significance (correlation = 0.6). **(c, d)** Linear regression between the wind stress and significant wave height at 18 hours before peak **(b)** (r^2=.58, p < 0.01) and 0 hours **(c)** (regression was not significant).
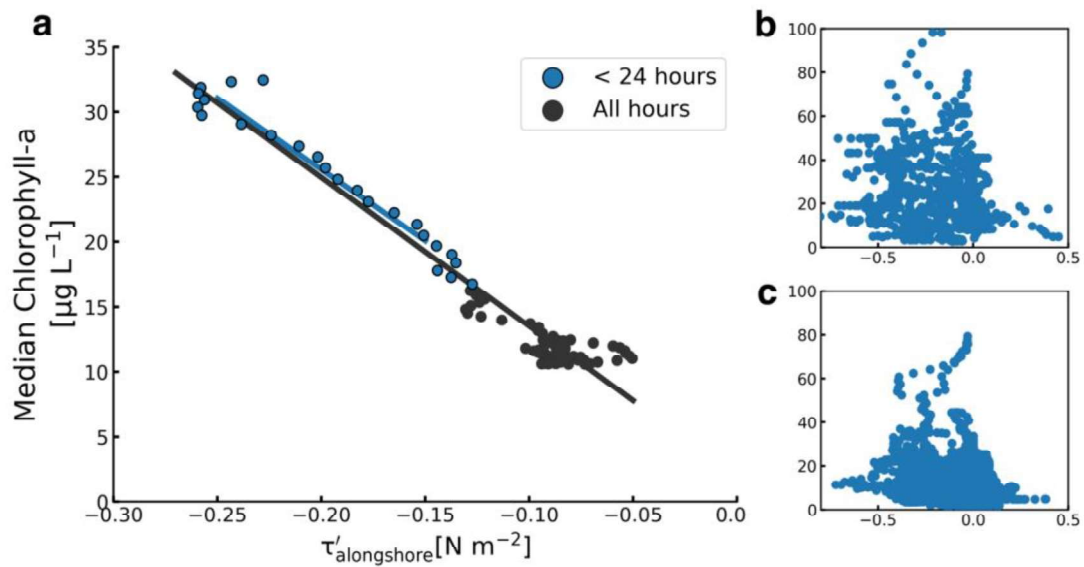
Figure 10. Regression of the conditional average of alongshore wind stress and intertidal chlorophyll-a. **(a)** Linear regression of only values within 24 hours before peak (blue line, blue filled circles) reveals a slightly better fit ($r^2 = 0.93$, p = > 0.01) than a linear regression of the entire 96-hour timeseries (blue line, $r^2 = 0.88$, p = > 0.01). **(b,c)** Same axes as **(a)**, showing all of the data within 24 hours of the peak **(b)** and from 24-70 hours before peak **(b).**
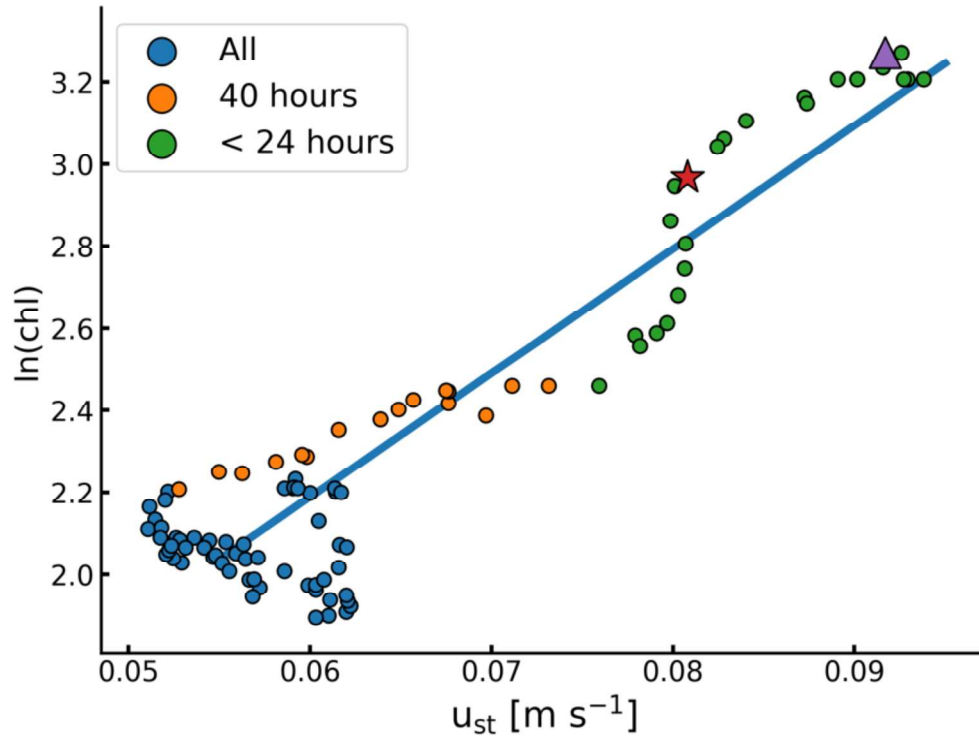
Figure 11. A linear regression (r^2=.812, p < 0.01) of the natural log of median intertidal chlorophyll against the magnitude of stokes drift, calculated from offshore *in situ* wave buoys. Orange filled circles are values that occurred between 40 and 24 hours of the peak of chlorophyll. Green circles are values that occurred with 24 hours of the peak. Conditions at the peak (hours before=0) is denoted by a red triangle. Conditions at 13 hours before the peak is denoted by a red star.
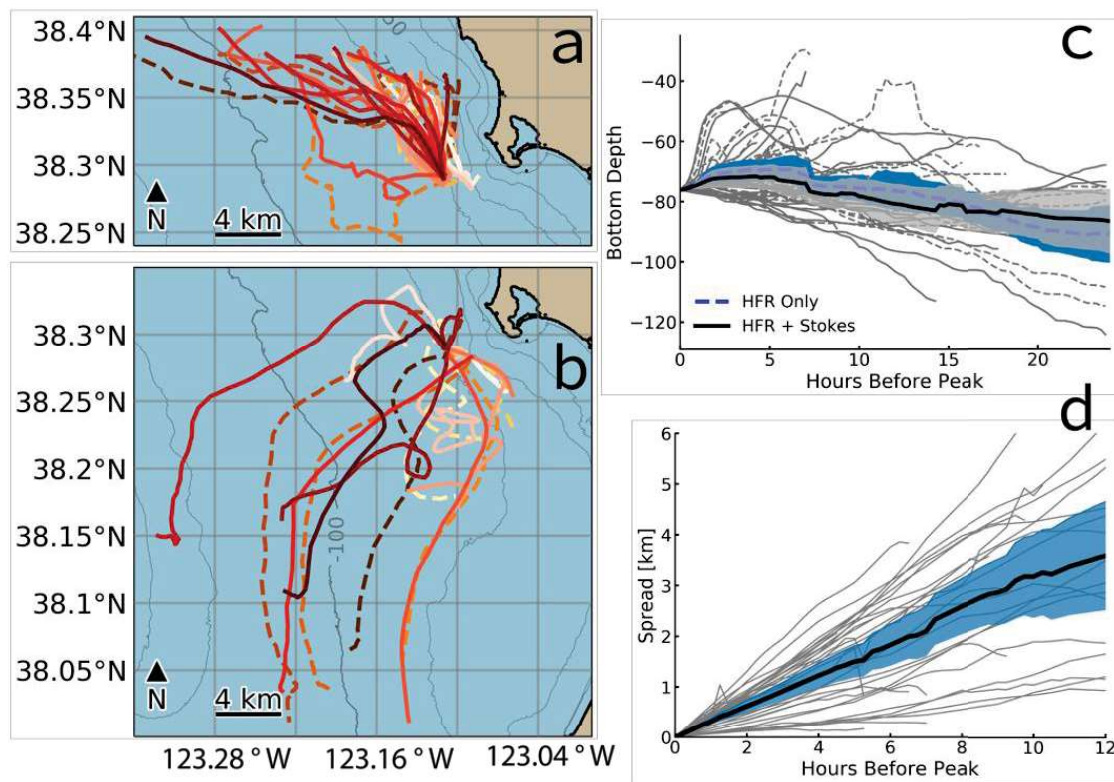
Figure 12. (a, b) Reverse mean particle trajectories up to 48 hours before peak intertidal chlorophyll for each event broken out by whether or not the origin was North **(a, n=26)** or South **(b, n=8)** of the seeding position. Solid lines indicate mean particle trajectories calculated from HFR-derived surface currents with Surface stokes drift term added. Dashed lines indicate mean particle trajectories calculated from HFR-derived surface currents only. **(c)** Bottom depth [units: meters] at the each timestep of the mean particle trajectories forced with HFR-derived surface currents + Surface Stokes (solid grey line) and HFR-derived surface currents only (dashed grey line). Mean bottom depth with 95% confidence around the mean for HFR-derived surface currents + Surface Stokes (solid black line) and HFR-derived surface currents only (dashed blue line). **(d)** Spread, as measured as the distance between mean particle trajectory position calculated from HFR-derived surface currents + Surface Stokes and HFR-derived surface currents only. Mean value (solid black line) with 95% confidence around the mean (blue shading).

	n	Mean		Median		S.D.	
		13 Hr	**48 Hr**	**13 Hrs**	**48 Hrs**	**13 Hrs**	**48 Hrs**
Chl-a Intertidal	**41**	**23.36**	**9.98**	**19.45**	**8.04**	13.95	9.1933
Temp Intertidal	**34**	**11.01**	**10.72**	**10.39**	**10.43**	1.4383	1.5469
u_{ss} **- Offshore**	**41**	**0.081**	**0.053**	**0.075**	**0.043**	0.0417	0.0355
u_{ss} **- Mops**	**41**	**0.237**	**0.22**	**0.06**	**0.035**	0.3811	0.3887
Wind Stress	**41**	0.201	0.083	0.144	0.0482	0.1625	0.0878
u_{E} Hfr	**24**	0.266	0.156	0.243	0.1218	0.1414	0.0869
Hs	**41**	2.568	1.861	2.455	1.805	0.7989	0.6654

Table 1. Summary statistics of different conditional averages from 13 hours before the peak (maximum dChl/dt) and 48 hours before the peak. Bold values indicate parameters where a Shapiro-Wilk test rejected the null hypothesis ($p < 0.05$) that data were normally were drawn from a normal distribution.

REFERENCES

Carr, M.-E. (2001). Estimation of potential productivity in Eastern Boundary Currents using remote sensing. Deep Sea Research Part II: Topical Studies in Oceanography, 49(1–3), 59–80. https://doi.org/10.1016/S0967-0645(01)00094-7

Calbet, A., & Landry, M. R. (2004). Phytoplankton growth, microzooplankton grazing, and carbon cycling in marine systems. *Limnology and Oceanography*, *49*(1), 51–57. https://doi.org/10.4319/lo.2004.49.1.0051

Cianelli, D., D'Alelio, D., Uttieri, M., Sarno, D., Zingone, A., Zambianchi, E., & D'Alcalà, M. R. (2017). Disentangling physical and biological drivers of phytoplankton dynamics in a coastal system. Scientific Reports, 7(1), 1–15. https://doi.org/10.1038/s41598-017-15880-x

Clarke, A. J., & Van Gorder, S. (2018). The Relationship of Near-Surface Flow, Stokes Drift and the Wind Stress. *Journal of Geophysical Research: Oceans*, *4560*, 1–13. https://doi.org/10.1029/2018JC014102

Dagestad, K.-F., Röhrs, J., Breivik, Ø., & Ådlandsvik, B. (2018). OpenDrift v1.0: a generic framework for trajectory modelling. *Geoscientific Model Development*, *11*(4), 1405–1420. https://doi.org/10.5194/gmd-11-1405-2018

Dever, E. P., Dorman, C. E., & Largier, J. L. (2006). Surface boundary-layer variability off Northern California, USA, during upwelling. *Deep-Sea Research Part II: Topical Studies in Oceanography*, *53*(25–26), 2887–2905. https://doi.org/10.1016/j.dsr2.2006.09.001

Earle, M. D. (1996). Nondirectional and directional wave data analysis procedures. NDBC Technical Document 96 (Vol. 002).

Earle, M. D., Steele, K. E., & Wang, D. W. C. (1999). Use of advanced directional wave spectra analysis methods. Ocean Engineering, 26(26), 1421–1434. https://doi.org/10.1016/S0029-8018(99)00010-4

García-Reyes, M., & Largier, J. L. (2012). Seasonality of coastal upwelling off central and northern California: New insights, including temporal and spatial variability. Journal of Geophysical Research: Oceans, 117(C3), n/a-n/a. https://doi.org/10.1029/2011JC007629

Graham, W. M., & Largier, J. L. (1997). Upwelling shadows as nearshore retention sites: The example of northern Monterey Bay. *Continental Shelf Research*, *17*(5), 509–532. https://doi.org/10.1016/S0278-4343(96)00045-3

Halle, C. M., & Largier, J. L. (2011). Surface circulation downstream of the Point Arena upwelling center. *Continental Shelf Research*, *31*(12), 1260–1272. https://doi.org/10.1016/j.csr.2011.04.007

Huyer, A. (1983). Coastal upwelling in the California current system. Progress in Oceanography, 12(3), 259–284. https://doi.org/10.1016/0079-6611(83)90010-1

Kaplan, D. M., & Largier, J. (2006). HF radar-derived origin and destination of surface waters off Bodega Bay, California. *Deep-Sea Research Part II: Topical Studies in Oceanography*, *53*(25–26), 2906–2930. https://doi.org/10.1016/j.dsr2.2006.07.012

Kirincich, A. R., Lentz, S. J. & Barth, J. a. Wave-Driven Inner-Shelf Motions on the Oregon Coast. J. Phys. Oceanogr. 39, 2942–2956 (2009).

Kumar, N., Cahl, D. L., Crosby, S. C., & Voulgaris, G. (2017). Bulk versus Spectral Wave Parameters: Implications on Stokes Drift Estimates, Regional Wave Modeling, and HF Radars Applications. Journal of Physical Oceanography, 47(6), 1413–1431. https://doi.org/10.1175/JPO-D-16-0203.1

Large, W. G., & Pond, S. (1981). Open Ocean Momentum Flux Measurements in Moderate to Strong Winds. Journal of Physical Oceanography. https://doi.org/10.1175/1520-0485(1981)011<0324:OOMFMI>2.0.CO;2

Lentz, S. J., Fewings, M., Howd, P., Fredericks, J., & Hathaway, K. (2008). Observations and a Model of Undertow over the Inner Continental Shelf. *Journal of Physical Oceanography*, *38*(11), 2341–2357. https://doi.org/10.1175/2008JPO3986.1

Lentz, S. J. & Fewings, M. R. The Wind- and Wave-Driven Inner-Shelf Circulation. Ann. Rev. Mar. Sci. 4, 317–343 (2012).

McPhee-Shaw, E. E., Nielsen, K. J., Largier, J. L., & Menge, B. A. (2011). Nearshore chlorophyll-a events and wave-driven transport. Geophysical Research Letters, 38(2). https://doi.org/10.1029/2010GL045810

McWilliams, J. C., & Restrepo, J. M. (1999). The Wave-Driven Ocean Circulation. *Journal of Physical Oceanography*, *29*(10), 2523–2540. https://doi.org/10.1175/1520-0485(1999)029<2523:TWDOC>2.0.CO;2

Menge, B. A., & Menge, D. N. L. (2013). Dynamics of coastal meta-ecosystems: the intermittent upwelling hypothesis and a test in rocky intertidal regions. Ecological Monographs, 83(3), 283–310. https://doi.org/10.1890/12-1706.1

Monismith, S. G., & Fong, D. A. (2004). A note on the potential transport of scalars and organisms by surface waves. Limnology and Oceanography, 49(4), 1214–1217. https://doi.org/10.4319/lo.2004.49.4.1214

Morgan, S. G., Shanks, A. L., MacMahan, J. H., Reniers, A. J. H. M., & Feddersen, F. (2018). Planktonic Subsidies to Surf-Zone and Intertidal Communities. *Annual Review of Marine Science*, *10*(1). https://doi.org/10.1146/annurev-marine-010816-060514

Nickols, K., Miller, S., Gaylord, B., Morgan, S., & Largier, J. (2013). Spatial differences in larval abundance within the coastal boundary layer impact supply to shoreline habitats. Marine Ecology Progress Series, 494, 191–203. https://doi.org/10.3354/meps10572

National Geophysical Data Center, 2003. U.S. Coastal Relief Model - Central Pacific. National Geophysical Data Center, NOAA. doi:10.7289/V50Z7152 [2018-05-01]

O'Reilly, W. C., Herbers, T. H. C., Seymour, R. J., & Guza, R. T. (1996). A Comparison of Directional Buoy and Fixed Platform Measurements Of Pacific Swell. Journal of Atmospheric and Oceanic Technology, 13(1), 231–238. https://doi.org/10.1175/1520-0426(1996)013<0231:ACODBA>2.0.CO;2

O'Reilly, W. C., Olfe, C. B., Thomas, J., Seymour, R. J., & Guza, R. T. (2016). The California coastal wave monitoring and prediction system. Coastal Engineering, 116, 118–132. https://doi.org/10.1016/j.coastaleng.2016.06.005

Paquin, A. L. (2012). Seasonal and event scale forcing of phytoplankton abundance and taxonomic composition in the surfzone of an open-coast, rocky shore. Master's Thesis Sonoma State University.

Paduan, J. D., & Washburn, L. (2013). High-Frequency Radar Observations of Ocean Surface Currents. *Annual Review of Marine Science*, *5*(1), 115–136. https://doi.org/10.1146/annurev-marine-121211-172315

Paduan, J. D., Cook, M. S., & Tapia, V. M. (2016). Patterns of upwelling and relaxation around Monterey Bay based on long-term observations of surface currents from high frequency radar. *Deep Sea Research Part II: Topical Studies in Oceanography*, *151*, 129–136. https://doi.org/10.1016/j.dsr2.2016.10.007

Pauly, D., & Christensen, V. (1995). Primary production required to sustain global fisheries. Nature, 374(6519), 255–257. https://doi.org/10.1038/374255a0

Pickett, M. H., Paduan, J. D. (2003). Ekman transport and pumping in the California Current based on the U.S. Navy's high-resolution atmospheric model (COAMPS). Journal of Geophysical Research, 108(C10), 3327. https://doi.org/10.1029/2003JC001902

Pickett, M. H., & Schwing, F. B. (2006). Evaluating upwelling estimates off the west coasts of North and South America. *Fisheries Oceanography*, *15*(3), 256–269. https://doi.org/10.1111/j.1365-2419.2005.00400.x

Ren, L., Hu, Z., & Hartnett, M. (2018). Short-Term Forecasting of Coastal Surface Currents Using High Frequency Radar Data and Artificial Neural Networks. *Remote Sensing*, *10*(6), 850. https://doi.org/10.3390/rs10060850

Renault, L., Deutsch, C., McWilliams, J. C., Frenzel, H., Liang, J. H., & Colas, F. (2016). Partial decoupling of primary productivity from upwelling in the California Current system. *Nature Geoscience*, *9*(7), 505–508. https://doi.org/10.1038/ngeo2722

Röhrs, J., Christensen, K. H., Hole, L. R., Broström, G., Drivdal, M., & Sundby, S. (2012). Observation-based evaluation of surface wave effects on currents and trajectory forecasts. Ocean Dynamics, 62(10–12), 1519–1533. https://doi.org/10.1007/s10236-012-0576-y

Röhrs, J., Sperrevik, A. K., Christensen, K. H., Broström, G., & Breivik, Ø. (2015). Comparison of HF radar measurements with Eulerian and Lagrangian surface currents. *Ocean Dynamics*, *65*(5), 679–690. https://doi.org/10.1007/s10236-015-0828-8

Saha, D., Deo, M. C., & Bhargava, K. (2016). Interpolation of the gaps in current maps generated by high-frequency radar. International Journal of Remote Sensing, 37(21), 5135–5154. https://doi.org/10.1080/01431161.2016.1230281

Shanks, A. L., Morgan, S. G., MacMahan, J., Reniers, A. J. H. M., Jarvis, M., Brown, J., Griesemer, C. (2018). Persistent Differences in Horizontal Gradients in Phytoplankton Concentration Maintained by Surf Zone Hydrodynamics. *Estuaries and Coasts*, *41*(1), 158–176. https://doi.org/10.1007/s12237-017-0278-2

Shadden, S. C., Lekien, F., Paduan, J. D., Chavez, F. P. & Marsden, J. E. The correlation between surface drifters and coherent structures based on high-frequency radar data in Monterey Bay. *Deep Sea Res. Part II Top. Stud. Oceanogr.* 56, 161–172 (2009).

Solabarrieta, L. *et al.* Skill assessment of HF radar-derived products for Lagrangian simulations in the Bay Of Biscay. *J. Atmos. Ocean. Technol.* 33, 2585–2597 (2016).

Stokes, G. (1880). On the Theory of Oscillatory Waves. In *Mathematical and Physical Papers* (Cambridge Library Collection - Mathematics, pp. 197-229). Cambridge: Cambridge University Press. doi:10.1017/CBO9780511702242.013

Tamura, H., Miyazawa, Y., & Oey, L.-Y. (2012). The Stokes drift and wave induced-mass flux in the North Pacific. Journal of Geophysical Research: Oceans, 117(C8). https://doi.org/10.1029/2012JC008113

Thompson, R. O. R. Y. (1983). Low-Pass Filters to Suppress Inertial and Tidal Frequencies. *Journal of Physical Oceanography*, *13*(6), 1077–1083. https://doi.org/10.1175/1520-0485(1983)013<1077:LPFTSI>2.0.CO;2

Wang, X., Chao, Y., Dong, C., Farrara, J., Li, Z., McWilliams, J. C., Paduan, J. D., Rosenfeld, L. K. (2009). Modeling tides in Monterey Bay, California. *Deep-Sea Research Part II: Topical Studies in Oceanography*, *56*(3–5) 219–231 https://doi.org/10.1016/j.dsr2.2008.08.012

Webb, A., & Fox-Kemper, B. (2011). Wave spectral moments and Stokes drift estimation. *Ocean Modelling*, *40*(3–4), 273–288. https://doi.org/10.1016/j.ocemod.2011.08.007

Wieters, E., Kaplan, D., Navarrete, S., Sotomayor, A., Largier, J., Nielsen, K., & Véliz, F. (2003). Alongshore and temporal variability in chlorophyll a concentration in Chilean nearshore waters. Marine Ecology Progress Series, 249, 93–1